Electronic Supplementary Information

A Strain-Reinforcing Elastomer Adhesive with Superior Adhesive Strength and Toughness

Chuanlong Li[a], Wenbo Dong[a], Longyu Li[a], Zhengli Dou[a], Yuhan Li[b], Liuhe Wei[b], Qin Zhang*[a], Qiang Fu[a] and Kai Wu*[a]

[a.] College of Polymer Science and Engineering, State Key Laboratory of Polymer Materials Engineering, Sichuan University, Chengdu 610065, PR China.

[b.] College of Chemistry and Green Catalysis Center, Zhengzhou Key Laboratory of Elastic Sealing Materials, Zhengzhou University, Zhengzhou 450001, PR China

*Corresponding authors: Kai Wu, e-mail: kaiwu@scu.edu.cn and Qin Zhang, e-mail: qinzhang@scu.edu.cn

Synthesis of chain extender

The chain extender that contains adhesive unit (DMPA-DA) was synthesized according to Fig. S1, which includes the following four steps:

(1) Synthesis of DMPA-D: DMPA (13.41 g, 100 mmol) and DMP (13.54 g, 130 mmol) were dissolved in acetone, then TsOH (0.1 g, 0.53 mmol) was added into the solution. After stirring for 11 h at room temperature, 1 mL ammonium hydroxide-ethanol mixture (v/v = 1:1) was added into the solution to neutralize the mixture. Then, the solution was stirred for another 20 min and the residual solid was removed by filtration. The filtrate was evaporated by rotary evaporator. The crude product was dissolved in DCM and washed three times with deionized water. Finally, the organic phase was concentrated to dryness and the product was dried under vacuum conditions at 60 ^{o}C overnight. The obtained DMPA-D was a white solid with a yield of 87.3 % (15.2 g). ^{1}H nuclear magnetic resonance (NMR) spectrum of DMPA-D was shown in Fig. S2.

(2) Synthesis of DMPA-D-NHS: DMPA-D (8.71 g, 50 mmol) and NHS (6.90 g, 60 mmol) were dissolved in DCM, then EDC-HCl (23.00g, 120 mmol) was added into the solution. The mixture was first stirred at 0 ^{o}C for 2 h and then at room temperature for 25 h. Next, the solution was washed with saturated NaHCO$_3$ solution, dilute hydrochloric acid solution and deionized water 3 times, respectively. Finally, the organic phase was concentrated to dryness and the product was dried under vacuum at 60 °C overnight to obtain DMPA-D-NHS with a yield of 86.4 % (11.7 g). ^{1}H NMR spectrum of DMPA-D-NHS was shown in Fig. S3.

(3) Synthesis of DMPA-D-DA: DMPA-D-NHS (5.43 g, 20 mmol) and dopamine hydrochloride (DA-HCl, 5.69 g, 30 mmol) were added into a 250 mL three-neck flask under nitrogen with magnetic stirring, followed by the addition of 70 mL DCM and 70 mL methanol. Next, triethylamine (3.04 g, 30 mmol) was added, and the reaction was performed for 24 h at 0 ^{o}C. Then, the mixed solution was evaporated by rotary evaporator to obtain a yellow viscous material. The viscous material was washed with 0.1 M hydrochloric acid and a large white precipitate appeared at the bottom of the solution, which was collected and freeze-dried to obtain DMPA-D-DA with a yield of 90.5 % (5.6 g). ^{1}H NMR spectrum of DMPA-D-DA was shown in Fig. S4.

(4) Synthesis of DMPA-DA: DMP-DMPA-DA (4.64 g, 15 mmol) was added to the 150 mL three-neck flasks under nitrogen. Then, 100 mL of methanol and trifluoroacetic acid (1.71 g, 15 mmol) were added to the flask and stirred for 16 h at 30 ^{o}C. The solution was then concentrated under vacuum to give the crude product, which was finally dried under vacuum at 80 ^{o}C for 24 h to give the brown solid product DMPA-DA with a yield of 89.3 % (3.6 g).^{1}H NMR spectrum of DMPA-DA was shown in Fig. S5.

General characterizations

^{1}H NMR spectra were measured by a Bruker AV III HD system (400 MHz). Attenuated total reflectance Fourier transform infrared (FT-IR) spectra of bulk film were performed on a Nicolet 6700 (Thermo Electron Corporation, USA). Variable-temperature FT-IR spectroscopy was performed on a Nicolet iS 50 (Thermo Electron Corporation, USA). The temperature was set to rise from 25 to 120 °C with 5 °C interval. Molecular weight information was obtained from gel permeation chromatography (GPC, Waters-1515, USA,) with DMF/LiBr (2 g/1000 mL) as the mobile phase at 40 ^{o}C and polymethyl methacrylate (PMMA) as the standards. The flow rate of the mobile phase was 1.0 ml/min. Differential scanning calorimetry (DSC) measurement was carried out using a DSC Q2000 (TA, USA) with a heating rate of 10 °C/min under nitrogen atmosphere. The morphology of micro-phase separation was detected by atomic force microscope (AFM, Smart SPM, AIST-NT, USA). Rheological behaviors were measured with a rotating rheometer of Anton Paar instrument (MCR302, Austria) using an 8 mm parallel plate-plate geometry. Frequency sweeps were carried out at a strain amplitude of 0.1% in the range of 0.1 to 100 Hz, and the temperature was accurately adjusted from 25 °C to 105 °C with a temperature interval of 5 °C. Master curves were constructed (25 °C as the reference) according to the principle of time-temperature superposition (TTS). Small-angle X-Ray scattering (SAXS) was carried on a Cu Kα X-ray radiation source (Xeuss 2.0, Xenocs, France). Exposure time to X-ray was 3 min for all the samples. Observation of the phenomenon of strain-induced crystalization was conducted on optical microscopy (OM, Olympus BX51, Japan). X-ray diffraction (XRD) measurements were performed on Rigaku Ultima IV using Cu Kα radiation (λ =0.1541 nm). Samples were pre-stretched to a specific strain and then fixed before X-ray exposure.

Mechanical characterization

Tensile tests were performed with a rate of 50 mm/min at 25 °C on a tensile tester (INSTRON, 5967, USA) loaded with a 500 N load cell. At least three dumbbell samples with a tensile size of 12 × 5 × 1 mm were tested, and their average value was given. For fracture tests, rectangular specimens with 10 × 5 × 1 mm dimensions were

stretched at a speed of 50 mm/min. The gauge length is 1 mm while the notch depth is 1 mm. And the fracture energy (W_b) was calculated by the following equation:

$$G_c = \frac{U(W_b)}{a_0 \times b_0}$$

Adhesive characterization

All the substrates were commercially available. The surfaces were cleaned to wipe off any oil or dush. The details are as follows: For the metal substrates (aluminum, stainless steel and copper), they were immersed in acetone for 1 hour. For glass, epoxy and nitrile rubber, the surfaces were cleaned with non-woven cloth soaked in acetone, repeating this process three times. Subsequently, all substrates were rinsed twice with water and dried in a blast oven at 60℃ for 2 hours.

Lap shear tests were performed by a tensile tester (INSTRON, 5967, USA) loaded with a 5000 N load cell with a strain rate of 5 mm/min. Adhesive films were cut into 25 mm × 12.5 mm and placed between two substrates (100 mm × 25 mm × 1.5 mm). The samples were held by two paper clips and placed in an oven at 120 °C for 2 hours, followed by cooling down to room temperature. The preload was removed during the lap-shear testing. And the energy release rate that is used to evaluate the energy-dissipating capability was calculated as:

$$G = \frac{(F/W)^2}{4Eh}$$

where F, E, h, and w are the maximum destructive force, Young's modulus, thickness, and width of adhesives, respectively.

Broad-frequency dielectric spectra characterization

Broad-frequency dielectric spectra measurements were performed by a Novocontrol Concept 80 Dielectric Spectrometer equipped with Quatro Cryosystem temperature control and Alpha impedance analyzer. The disk-shaped film with 10 mm diameter and 1 mm thickness was placed between two parallel electrodes. Frequency sweep mode was selected within the frequency range of from 10^{-1} to 10^6 Hz at each temperature from -100 to -70 °C with 10 °C intervals, with temperature stability better than 0.1 °C. To study the local dynamics of PUD materials (T < Tg), the Havriliak and Negami (HN) function was adopted to analyze the dielectric spectra. The complex dielectric permittivity (ε*) data as a function of frequency can be described by the following equation:

$$\varepsilon^*(\omega) = \varepsilon_\infty \frac{\Delta\varepsilon}{[1 + (i\omega\tau_{HN})^\alpha]^\beta}$$

where ε_∞ is the high-frequency limit of ε', $\Delta\varepsilon$ is the dielectric strength, and the τ_{HN} is the characteristic relaxation time. The α and β parameters (α <0, $\alpha\beta$≤1) are defined as the symmetrical and asymmetrical broadening of the loss peak. The relation between τ_{HN} and average relaxation time τ_{max} could be given by the following equation:

$$\tau_{max} = \tau_{HN}[sin\frac{\pi\alpha\beta}{2(1+\beta)}]^{\frac{1}{\alpha}}[sin\frac{\pi\alpha}{2(1+\beta)}]^{-\frac{1}{\alpha}}$$

$$f_{max} = \frac{1}{2\pi\tau_{max}}$$

where f_{max} is the frequency at which ε'' passes through the maximum value. The relation between τ and the temperature is Arrhenius-like and can be described by:

$$\tau_{max} = \tau_0 exp(\frac{E_a}{RT})$$

where E_a is the activation energy and τ_0 is a proportionality constant.

Molecular Simulation

The binding energy of different hydrogen bond donors and acceptors was computed using Materials Studio software. Density functional theory calculations were carried out to optimize model structures. The exchange-functional is treated using the generalized gradient approximation (GGA) of the Perdew-Burke-Ernzerhof (PBE) functional. The integration accuracy is set as fine, SCF tolerance is fine, and the basis set is DNP in Dmol3 code. Finally, the binding energy of different donors and acceptors was calculated by:

$$E = E_{total} - E_1 - E_2$$

where E_{total} is the energy of combined structure, E_1 is the energy of hydrogen bond donor and E_2 is the acceptor.
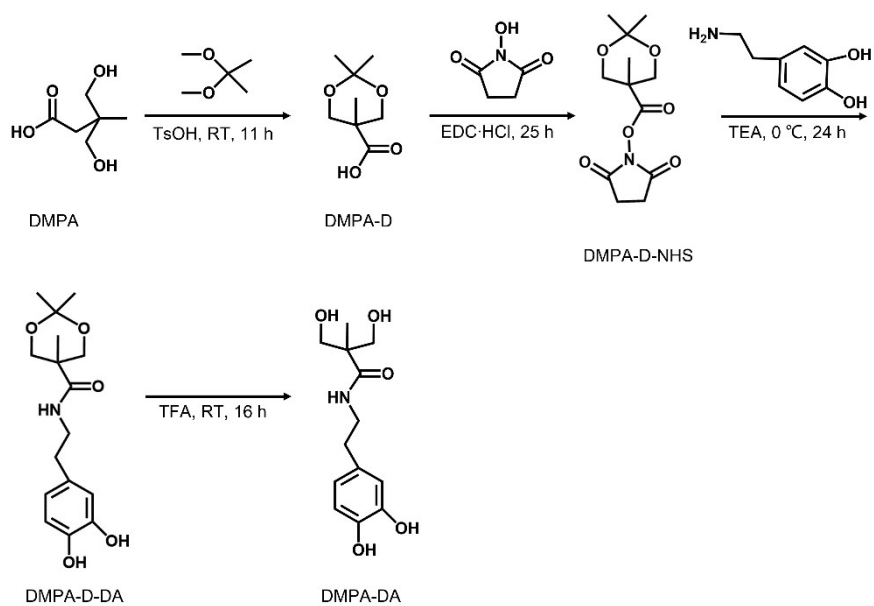
Fig. S1 Synthetic route of DMPA-DA chain extender.
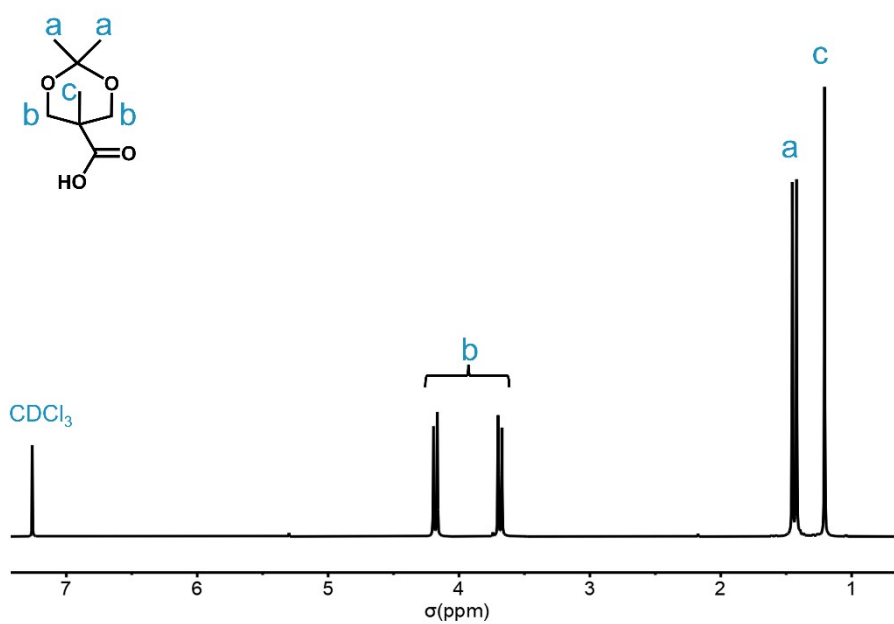

Fig. S2 ^{1}H nuclear magnetic resonance spectroscopy of DMPA-D (400 MHz, CDCl$_3$).
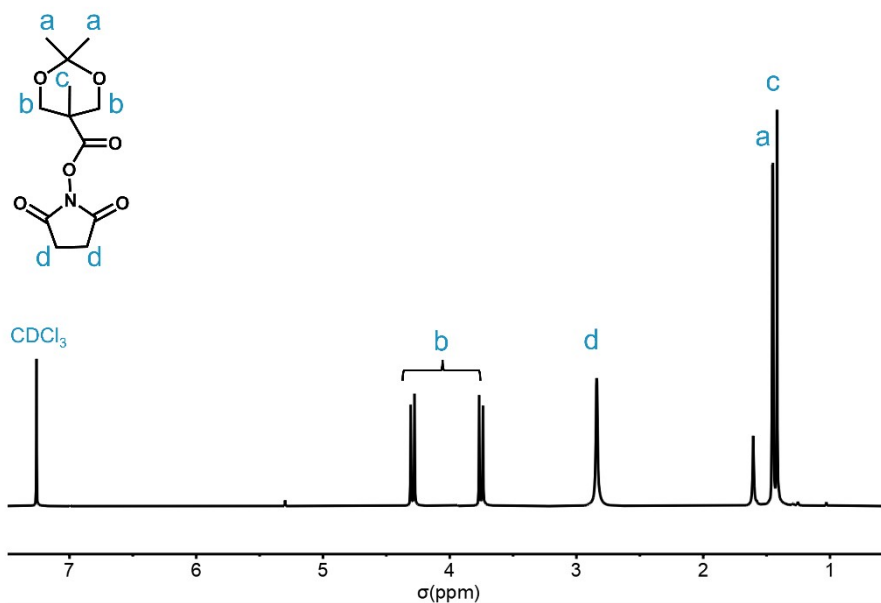
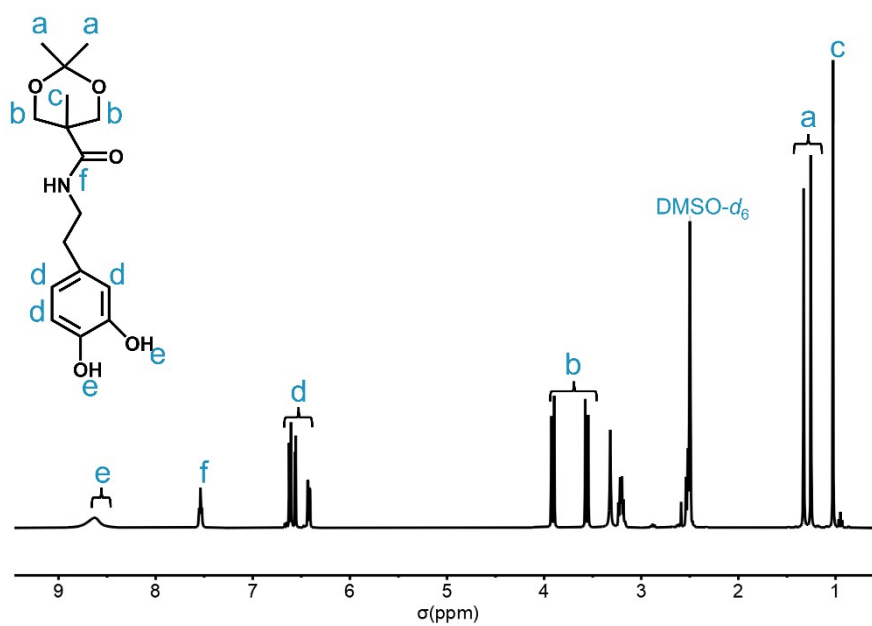**Fig. S3** ^{1}H nuclear magnetic resonance spectroscopy of DMPA-D-NHS (400 MHz, CDCl$_3$).

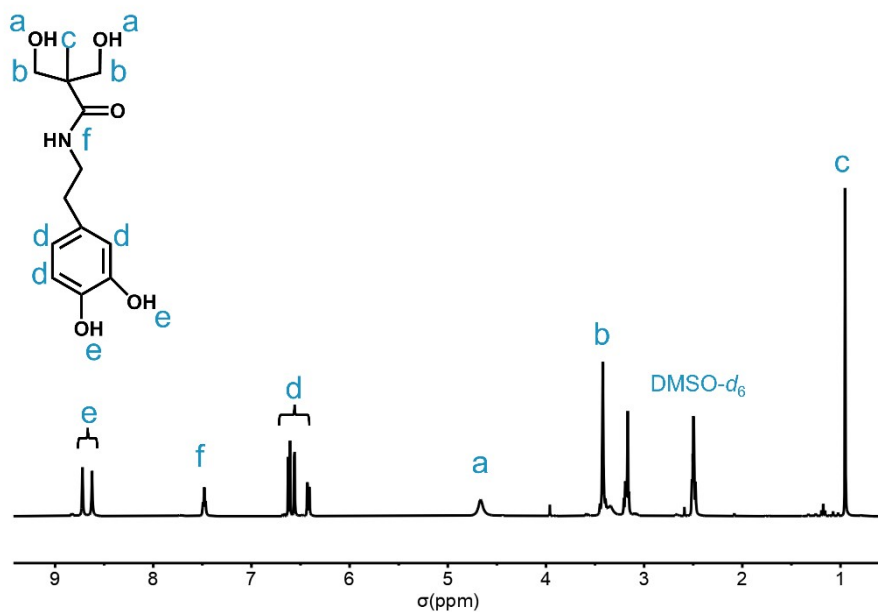**Fig. S4** ^{1}H nuclear magnetic resonance spectroscopy of DMPA-D-DA (400 MHz, DMSO-d_6).

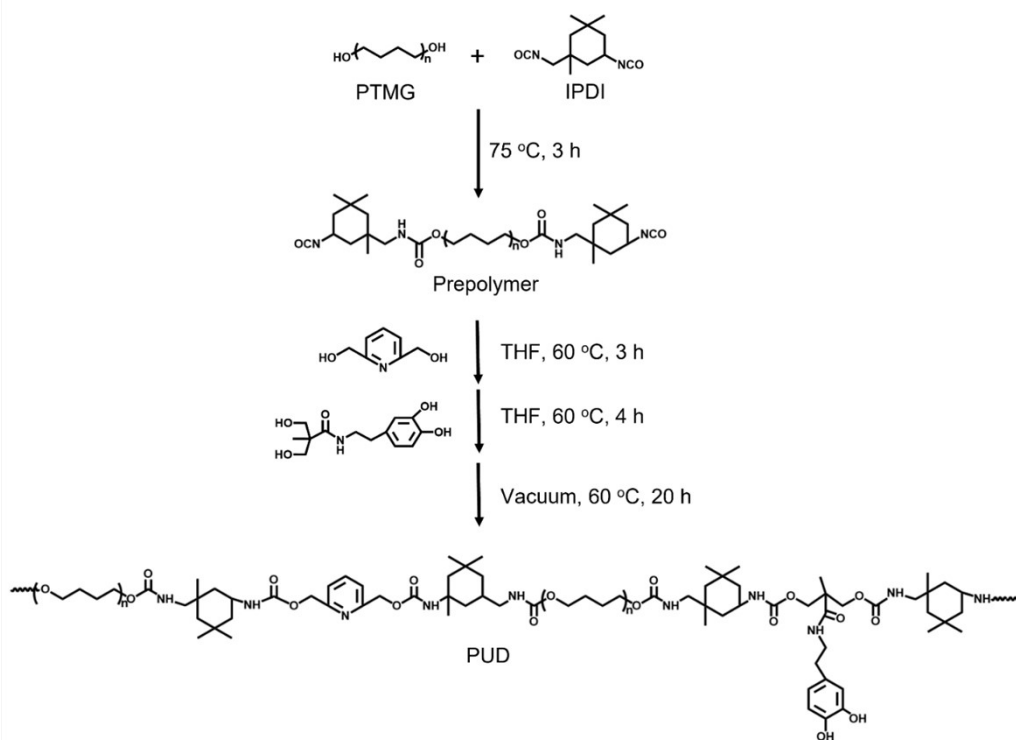**Fig. S5 ¹H nuclear magnetic resonance spectroscopy of DMPA-DA (400 MHz, DMSO-d_6).**

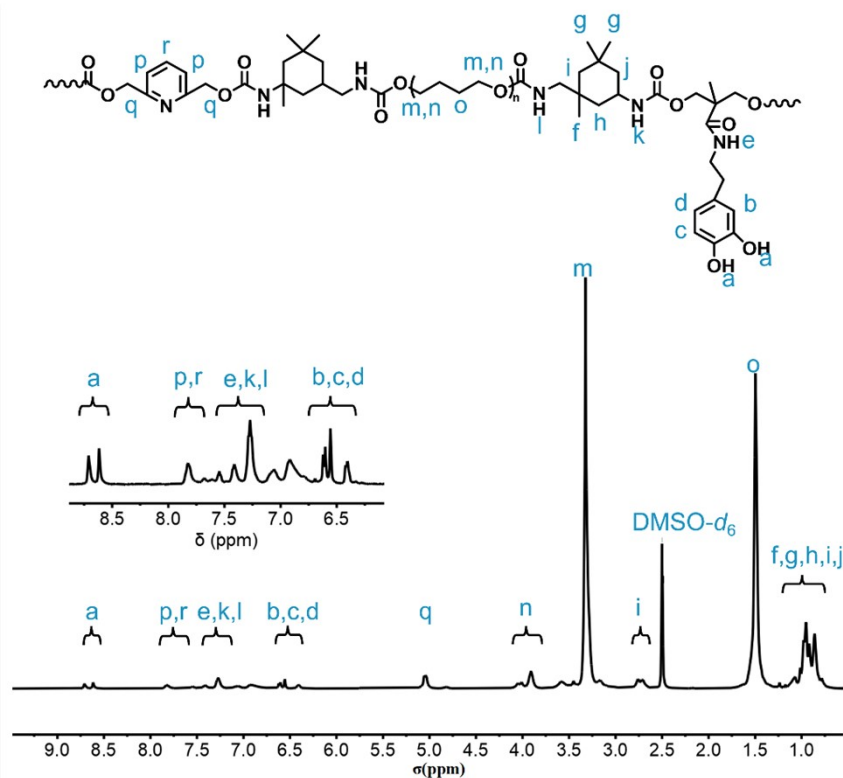**Fig. S6 Synthetic route of polyurethane adhesive (PUDx).**

Fig. S7 ^{1}H nuclear magnetic resonance spectroscopy of PUD20 (400 MHz, DMSO-d_6).
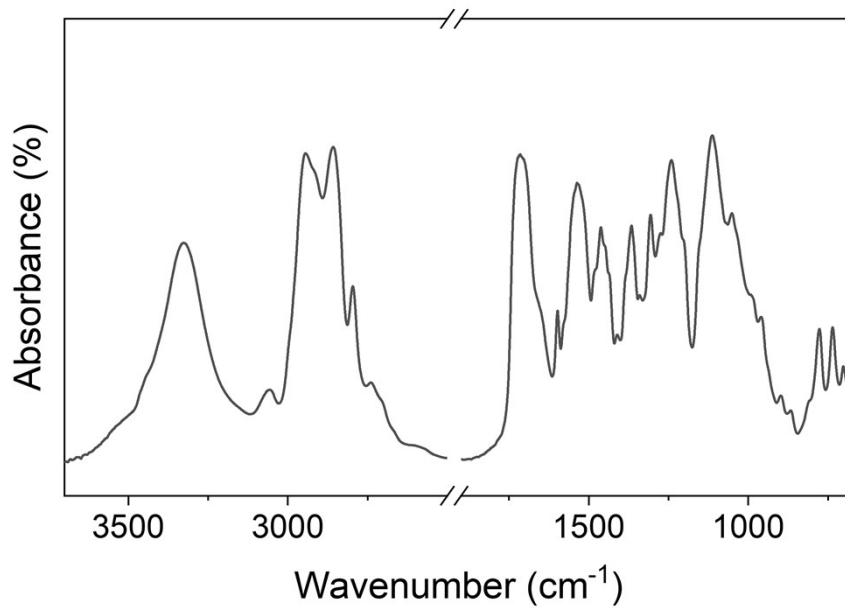

Fig. S8 Fourier transform infrared spectrum of PUD20. Detailed peak assignments are listed in Table S1.
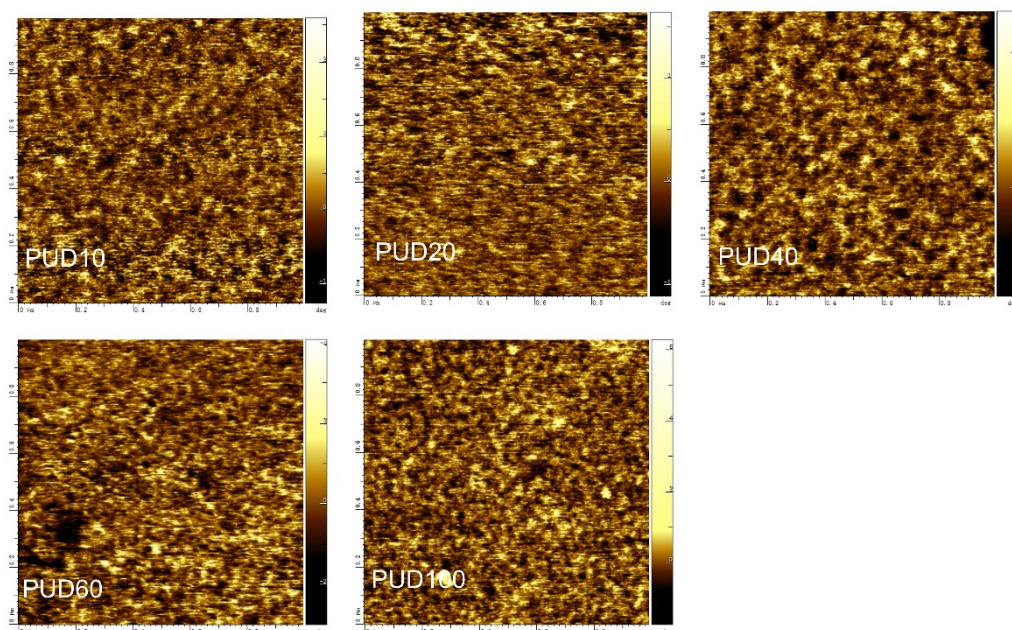
Fig. S9 Atomic force microscope phase images of the different PUDx materials. The images demonstrate a clear microphase-separation structure. The hard segment assembles into the loosely-packed nano-scale domain, which is visible as a bright color. In contrast, the soft domain represented by the dark color originates from the soft segment of PTMEG.
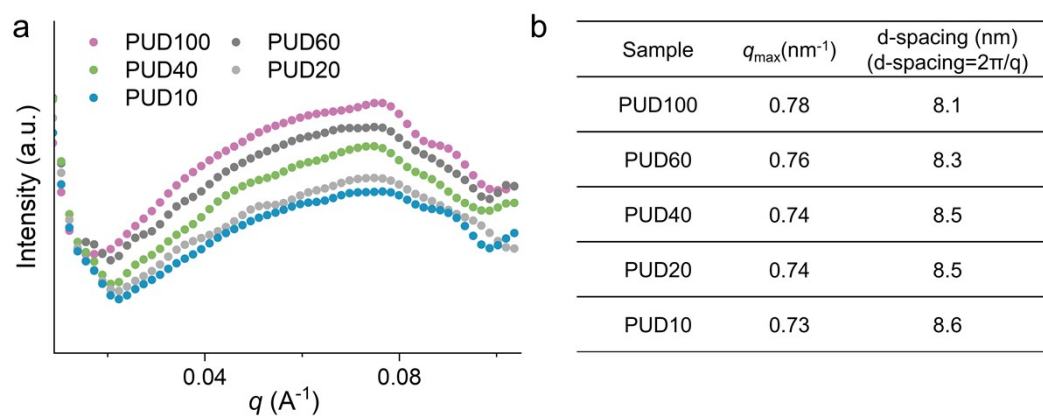

Sample	q_{max}(nm^{-1})	d-spacing (nm) (d-spacing=$2\pi/q$)
PUD100	0.78	8.1
PUD60	0.76	8.3
PUD40	0.74	8.5
PUD20	0.74	8.5
PUD10	0.73	8.6

Fig. S10 The microscope phase structure of the different PUDx materials. (a) Small angle X-ray scattering curves of the different PUDx materials. (b) Table concludes the calculation details about the q_{max} and d-spacing of the different PUDx materials. A broad scattering peak can be observed for each sample, which validates the microphase-separation structure. The peak of the q vector confirms that the hard segment assembles into the nano-scale domains.
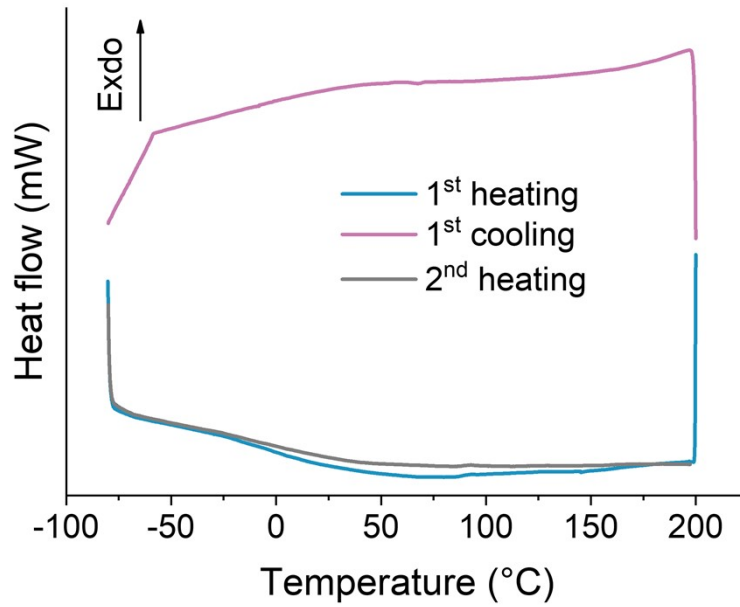
Fig. S11 Differential scanning calorimetry curve of PUD20 with the temperature increasing. The curve from -75 °C to 200 °C has no obvious step-change which is often regarded as the embodiment of the glass transition. But there is an obviously gentle slope in a wide range from -25 °C to 50 °C which is probably related to the hard domains with different bonding strengths and the randomly arranged soft segments. This heterogeneous structure imparts a distributed characteristic to the glass transition.
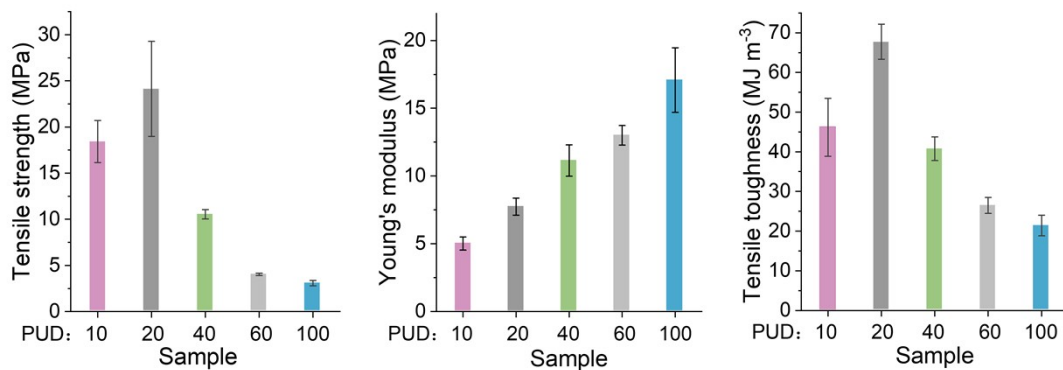

Fig. S12 Mechanical properties of the different PUDx adhesives. (a) Tensile strength, (b) Young's modulus, and (c) tensile toughness.
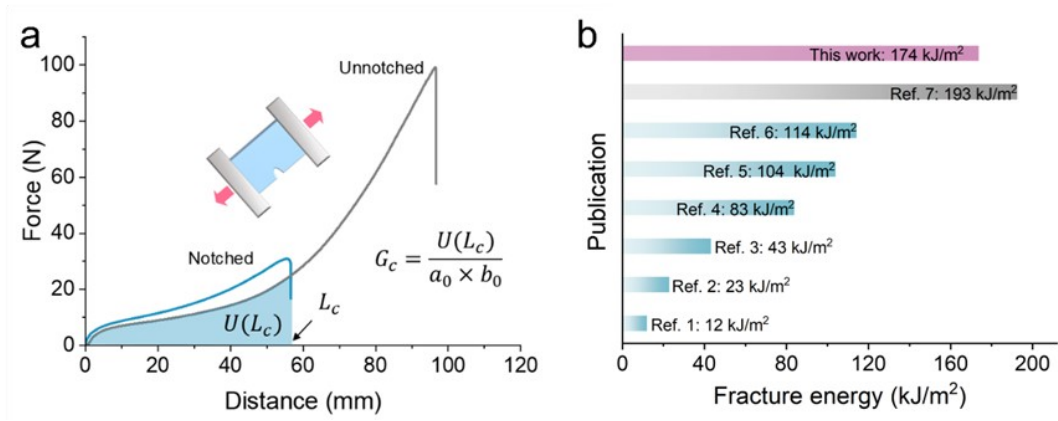
Fig. S13 Tensile stress–strain curves of the intact and notched PUD20. (a) Typical tensile force-displacement curves of the notched and unnotched PUD20. (b) Comparison of fracture energy of the PUD20 with other elastomers reported in the previous literature.[1-7]
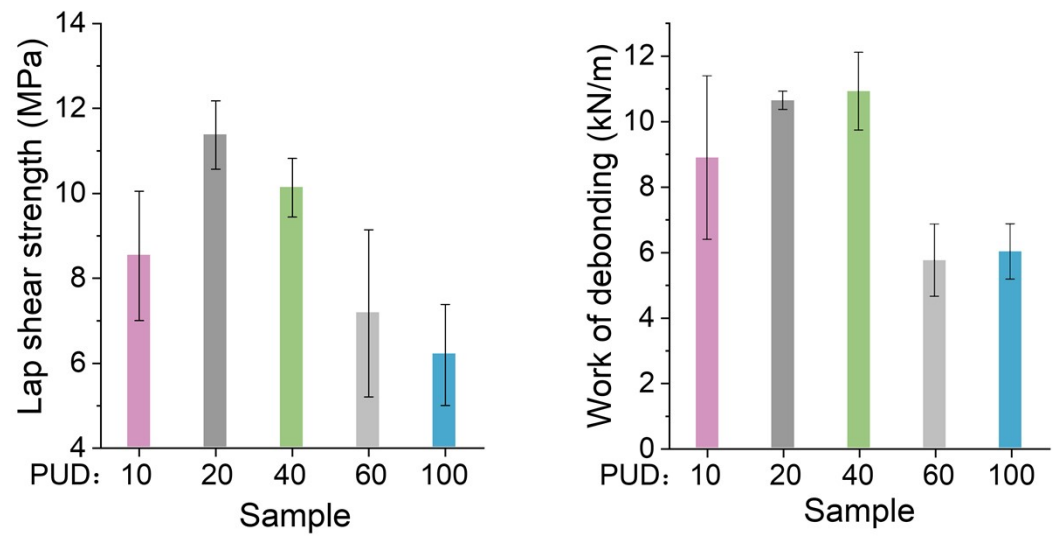

Fig. S 14 Lap shear strength of the different PUDx materials.
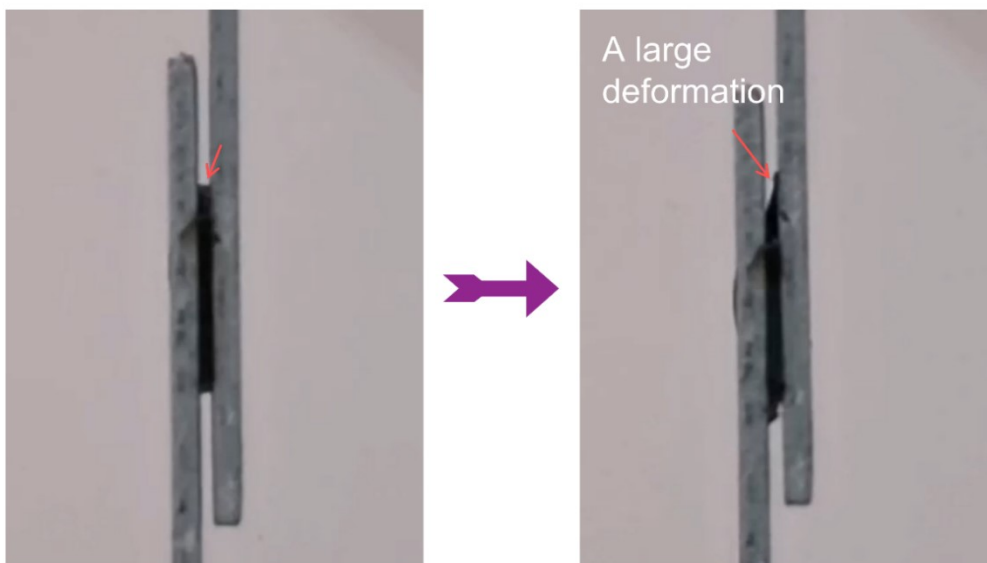
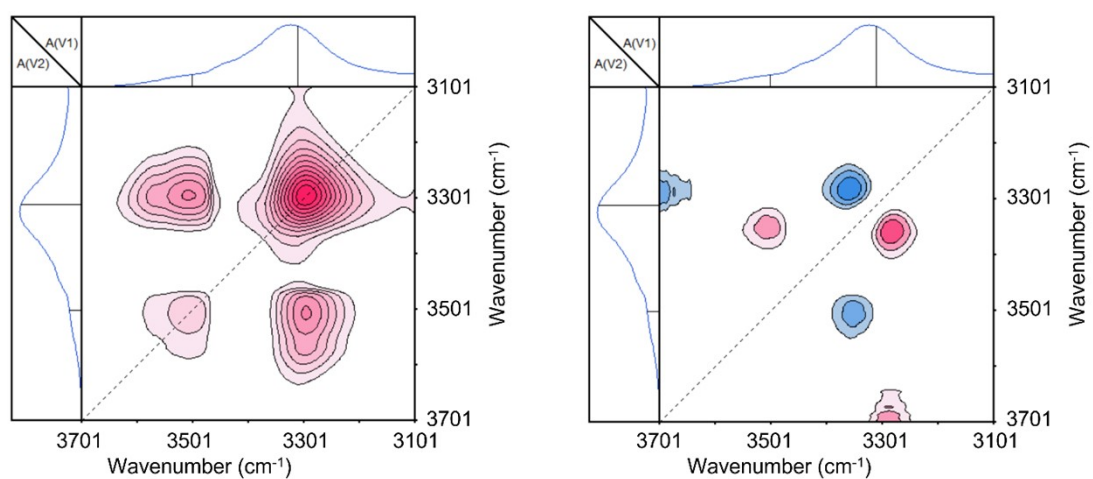**Fig. S15 Photographs showing the lap shear stretching process of the PUD20 material.**

Fig. S16 Synchronous and asynchronous two-dimensional Fourier transform infrared images of PUD20 with the wavenumber from 3702 to 3101 cm^{-1}.
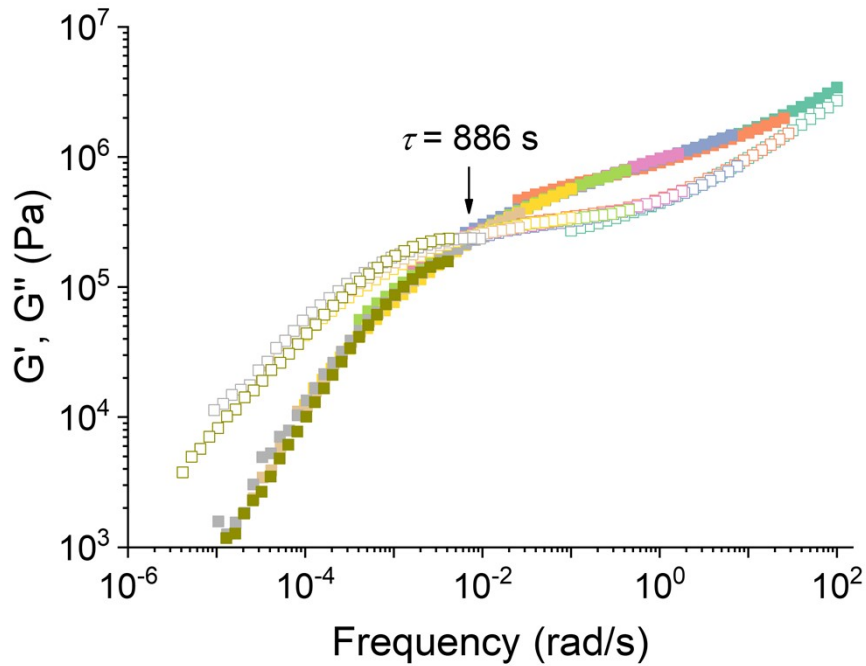
Fig. S17 Master curves of storage modulus (G') and loss modulus (G") obtained from rheology test for PUD20 at a reference temperature of 25 °C. The crossover point (ω_c) at G' = G" in the master curves is a symbolic transition of the adhesive network from a physically crosslinked and elastic state to a reversible and fluid-like state. The reciprocal of ω_c relates to the characteristic relaxation time (τ_c) that reflects the time it takes to perform such transition, and it can also be understood as a factor reflecting the chain mobility. The corresponding τ_c is 886 s.
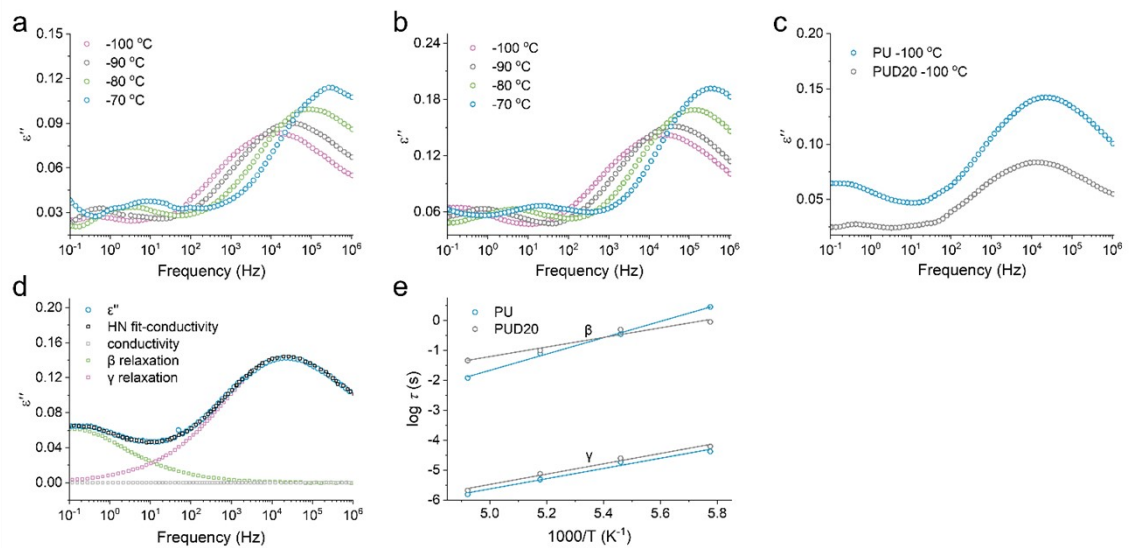
Fig. S18 Broad-frequency dielectric spectra of PUD20 and PU. Dielectric loss (ε'') of (a) PUD20 and (b) PU as a function of the frequency ranging from -100 to -70 °C. (c) Dielectric loss of PUD20 and PU as a function of the frequency at the typical temperature of -100 °C. (d) Dielectric loss spectra of PU fitted via a combination of three H-N equations with DC conductivity at -90 °C. (e) β and γ relaxation time for PUD20 and PU materials as a function of the temperature. The solid lines represent Arrhenius fittings for various relaxation processes.
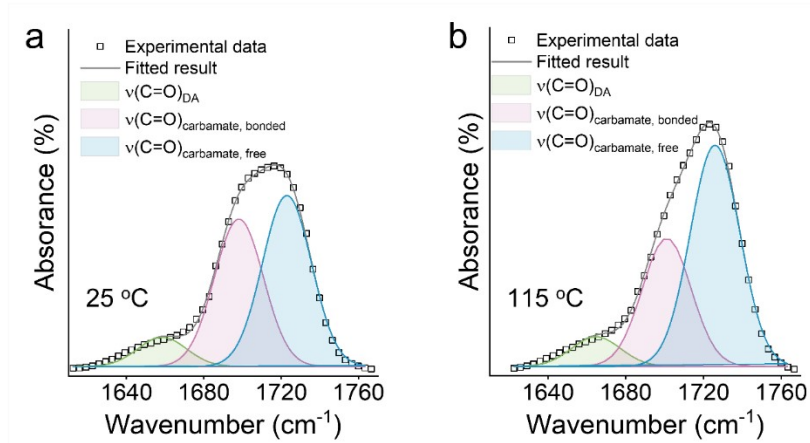
Fig. S19 Peak-splitting details of the ν(C=O) of the PUD20 material in the Fourier transform infrared spectra. (a) 25 °C, (b) 115 °C. The FTIR spectrum in the ν(C=O) of the PUD20 is carried out to further investigate the content variation of H-bonded moiety and free moiety as a function of temperature. It signifies that the shape of the peak gradually sharpens with the temperature increase. The C=O absorption band is further deconvoluted into three subpeaks for a more detailed investigation. These subpeaks are likely assigned to the DA, bonded C=O, and free C=O. And the bonded counterpart will gradually disassociate upon the temperature rising, and more and more C=O moiety will be free.
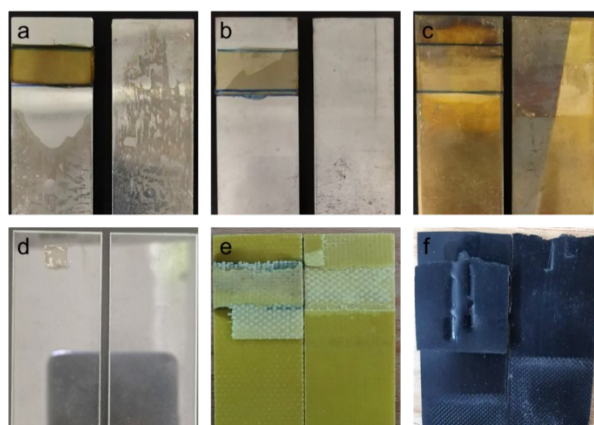
Fig. S20 Images showing the failure phenomenon of the different sandwiched substrates glued by the PUD20 adhesive: (a) aluminum, (b) stainless steel, (c) copper, (d) glass, (e) epoxy, (f) nitrile rubber. Noted that for the glass substrates, if using the 25 mm × 12.5 mm × 0.2 mm adhesive, the lap shear strength will be too large that the glass substrate will be totally broken. Therefore, a 6 mm × 6 mm × 0.2 mm adhesive was used to solve this issue.

2. Supplementary Tables

Table S1. Characteristic peak assignments of PUD20

Assignments	PUD20
	Wavenumber (cm^{-1})
v(N-H)	3328
v_a(CH$_2$)	2945
v_a(CH$_2$)	2910
v_s(CH$_2$)	2857
v_s(CH$_2$)	2794
v(C=O) amide I	1712
v(pyridine ring)	1598 and 1575
δ(N-H) amide II	1535
δ(N-H) amide III	1240
v(C-O-C)	1103

Table S2. Molecular weight information of the different PUDx materials

Sample	M_n (g/mol)	M_w (g/mol)	PDI[a]
PUD10	27300	60000	2.2
PUD20	32400	72000	2.2
PUD40	18800	42500	2.3
PUD60	15500	27700	1.8
PUD100	10200	28400	2.8

[a] polydispersity index.

Table S3. Comparison of the mechanical and adhesive properties of the PUDx materials with other reported adhesives in the previous studies

Type	Materials	Tensile strength (MPa)	Tensile toughness (kJ/m³)	Modulus (MPa)	Lap-shear strength (MPa)	Work of debonding (kN/m)	Debonding type	Substrate	Ref.
Gel	PAM/CNTs	0.017	0.061	/	0.025	/	/	Aluminum	[8]
	Tannic acid	0.054	0.44	/	0.048	/	/	Aluminum	[9]
	pHEAA	2.02	3.26	0.79	0.22	/	/	Glass	[10]
	Polyzwitterion/ clay	0.087	0.83	/	0.034	0.22	Cohesive failure	Glass	[11]
	PAA/Fe/Li	/	/	/	1.12	/	/	Glass	[12]
	Ionogel	/	/	/	0.43	5.48	Interfacial failure	Aluminum	[13]
	PDMS gel	/	/	/	0.22	0.12	/	Glass	[14]
Resin	Supramolecular EGTPA	6.19	/	/	6.02	/	/	Steel	[15]
	PC	/	/	/	4.28	/	/	Steel	[16]
	PC/H$_2$O	/	/	/	1.43	/	/	Aluminum	[17]
	Polypeptides/ surfactants	/	/	/	6.3	9.3	/	Steel	[18]
	Azobenzene Derivatives	/	/	/	1.34	1.36	Cohesive failure	Glass	[19]
	Supramolecule	11.75	0.72	343	14.6	6.32	/	Steel	[20]
	Ionic crystal	/	/	/	5.8	/	/	Glass	[21]
	Polymer/dendritic crystal	/	/	/	3.47	1.98	/	Glass	[22]
	Poly(ionic liquid)s	/	/	/	4.62	/	Interfacial and cohesive failure	Aluminum	[23]
	Epoxy resin	14.86	/	/	11.29	5.14	/	Aluminum	[24]
	Supramolecular epoxy	4.54	6.21	121.6	10.2	6.41	Interfacial and cohesive failure	Steel	[25]
Elastomer	Polyurethane	/	4.8	1.3	0.13	0.39	Interfacial failure	Glass	[26]
	Polyurethane	16.9	63.36	34.27	4.21	1.11	/	Steel	[27]
	Polyurethane	16.9	63.36	34.27	3.82	0.75	/	Glass	[27]
	Polyurethane	1.89	11.15	28.18	11.43	/	/	Aluminum	[28]
	Polyurethane	1.89	11.15	28.18	7.57	7.87	/	Steel	[28]
	Polyurethane	4.9	1.00	32.76	2.96	2.70	Cohesive failure	Steel	[29]
	Polyurethane	8.72	26.49	77.6	5.69	3.54	/	Steel	[30]
	Supramolecular elastomer	/	/	/	15.68	/	Interfacial failure	Steel	[31]
	Hyperbranched elastomer	1.24	0.65	4.52	6.49	4.44	Interfacial and cohesive failure	Aluminum	[32]
	Dynamically crosslinked nanocomposites	29	62.6	368	10.42	5.43	Interfacial and cohesive failure	Aluminum	[33]
	PUD10	18.43	46.17	5.01	8.52	7.92	/	Aluminum	This work
	PUD20	24.13	67.75	7.73	11.37	10.32	/	Aluminum	
	PUD40	10.54	40.75	11.14	10.13	10.45	/	Aluminum	
	PUD60	4.03	26.49	13.00	7.17	6.3	/	Aluminum	
	PUD100	3.08	21.42	17.08	6.19	6.12	/	Aluminum	

Abbreviations:

PAM- polyacrylamide; CNTs- carbon nanotubes; pHEAA- poly(N-hydroxyethyl acrylamide); PAA- poly(acrylic acid); PC- pillar[5]arene-crown ether

3. Supplementary Movies

Movie S1 This Movie showed that the deformation and debonding evolution process of PUD20 along the lap shear direction.

4. Supplementary References

1 J. Kang, D. Son, G. J. N. Wang, Y. Liu, J. Lopez, Y. Kim, J. Y. Oh, T. Katsumata, J. Mun, Y. Lee, *Adv.Mater.,* 2018, **30**, 1706846.

2 Y. Wang, X. Liu, S. Li, T. Li, Y. Song, Z. Li, W. Zhang, J. Sun, *ACS Appl. Mater. Interfaces,* 2017, **9**, 29120-29129.

3 X. Xun, X. Zhao, Q. Li, B. Zhao, T. Ouyang, Z. Zhang, Z. Kang, Q. Liao, Y. Zhang, *ACS nano,* 2021, **15**, 20656-20665.

4 X. Liu, X. Liu, W. Li, Y. Ru, Y. Li, A. Sun, L. Wei, *Chem. Eng. J.,* 2021, **410**, 128300.

5 Y. Li, W. Li, A. Sun, M. Jing, X. Liu, L. Wei, K. Wu, Q. Fu, *Mater. Horiz.,* 2021, **8**, 267-275.

6 F. Dong, X. Yang, L. Guo, Y. Wang, H. Shaghaleh, Z. Huang, X. Xu, S. Wang, H. Liu, *J. Mater. Chem. A,* 2022, **10**, 10139-10149.

7 X. Wang, S. Zhan, Z. Lu, J. Li, X. Yang, Y. Qiao, Y. Men, J. Sun, *Adv.Mater.,* 2020, **32**, 2005759.

8 Y. Li, D. Yang, Z. Wu, F.-L. Gao, X.-Z. Gao, H.-Y. Zhao, X. Li, Z.-Z. Yu, *Nano Energy,* 2023, 108324.

9 J. Mo, Y. Dai, C. Zhang, Y. Zhou, W. Li, Y. Song, C. Wu, Z. Wang, *Mater. Horiz.,* 2021, **8**, 3409-3416.

10 J. Xu, Z. Guo, Y. Chen, Y. Luo, S. Xie, Y. Zhang, H. Tan, L. Xu, J. Zheng, *Polymer,* 2021, **236**, 124321.

11 G. Gao, F. Yang, F. Zhou, J. He, W. Lu, P. Xiao, H. Yan, C. Pan, T. Chen, Z. L. Wang, *Adv.Mater.,* 2020, **32**, 2004290.

12 Y. Liu, P. Wang, X. Su, L. Xu, Z. Tian, H. Wang, G. Ji, J. Huang, *Adv. Mater.,* 2022, **34**, 2108820.

13 J. Zhu, X. Lu, W. Zhang, X. Liu, *Macromol. Rapid Commun.,* 2020, **41**, 2000098.

14 Y. Liu, G. Guan, Y. Li, J. Tan, P. Cheng, M. Yang, B. Li, Q. Wang, W. Zhong, K. Mequanint, *Sci.Adv.,* 2022, **8**, eabm9744.

15 M.-H. Zhang, C.-H. Li, J.-L. Zuo, *Chem. Eng. J.,* 2022, **433**, 133840.

16 X. Li, J. Lai, Y. Deng, J. Song, G. Zhao, S. Dong, *J. Am. Chem. Soc.,* 2020, **142**, 21522-21529.

17 T. Li, Q. Zhang, D. Li, S. Dong, W. Zhao, P. J. Stang, *ACS Appl. Mater. Interfaces,* 2020, **12**, 38700-38707.

18 J. Sun, L. Xiao, B. Li, K. Zhao, Z. Wang, Y. Zhou, C. Ma, J. Li, H. Zhang, A. Herrmann, K. Liu, *Angew. Chem. Int. Ed.,* 2021, **60**, 23687-23694.

19 Z. Wu, C. Ji, X. Zhao, Y. Han, K. MüLlen, K. Pan, M. Yin, *J. Am. Chem. Soc.,* 2019, **141**, 7385-7390.

20 P. Sun, S. Mei, J. F. Xu, X. Zhang, *Adv. Sci.,* 2022, **9**, 2203182.

21 L. Liu, Z. Liu, Y. Ren, X. Zou, W. Peng, W. Li, Y. Wu, S. Zheng, X. Wang, F. Yan, *Angew. Chem. Int. Ed.,* 2021, **133**, 9030-9041.

22 S. Xi, F. Tian, G. Wei, X. He, Y. Shang, Y. Ju, W. Li, Q. Lu, Q. Wang, *Adv.Mater.,* 2021, **33**, 2103174.

23 J. Zhang, Z. Chen, Y. Zhang, S. Dong, Y. Chen, S. Zhang, *Adv.Mater.,* 2021, **33**, 2100962.

24 W. Wang, Y. Li, H. Zhang, T. Chen, G. Sun, Y. Han, J. Li, *Biomacromolecules,* 2022, **23**, 779-788.

25 P. Sun, Y. Li, B. Qin, J.-F. Xu, X. Zhang, *ACS Mater. Lett.,* 2021, **3**, 1003-1009.

26 S. Wang, Y. Fang, H. He, L. Zhang, C. A. Li, J. Ouyang, *Adv. Funct. Mater.,* 2021, **31**, 2007495.

27 Z. H. Zhao, P. C. Zhao, Y. Zhao, J. L. Zuo, C. H. Li, *Adv. Funct. Mater.,* 2022, **32**, 2201959.

28 Y. Yao, Z. Xu, B. Liu, M. Xiao, J. Yang, W. Liu, *Adv. Funct. Mater.,* 2021, **31**, 2006944.

29 J. Yang, X. Zhou, J. Yang, J. Chen, Z. Sun, Y. Cheng, L. Yang, H. Wang, G. Zhang, J. Fu, *Chem. Eng. J.,* 2023, **451**, 138810.

30 S. Wang, Z. Liu, L. Zhang, Y. Guo, J. Song, J. Lou, Q. Guan, C. He, Z. You, *Mater. Chem. Front.,* 2019, **3**, 1833-1839.

31 S. Chen, Z. Li, Y. Wu, N. Mahmood, F. Lortie, J. Bernard, W. H. Binder, J. Zhu, *Angew. Chem. Int. Ed.,* 2022, **134**, e202203876.

32 H. Chen, H. Lin, Z. Sun, H. Li, C. He, D. Mao, *J. Mater. Chem. A,* 2023.

33 M. A. Rahman, C. Bowland, S. Ge, S. R. Acharya, S. Kim, V. R. Cooper, X. C. Chen, S. Irle, A. P. Sokolov, A. Savara, *Sci. Adv.,* 2021, **7**, eabk2451.